

# Calibration of *AstroSat*/UVIT Gratings and Spectral Responses

G. C. Dewangan<sup>1</sup>

<sup>1</sup>Inter-University Centre for Astronomy and Astrophysics (IUCAA), SPPU Campus, Pune, India.

\*Corresponding author. E-mail: gulabd@iucaa.in

MS received 7 November 2020; accepted 20 December 2020

**Abstract.** *AstroSat*/UVIT carries two gratings in the FUV channel and a single grating in the NUV channel. These gratings are useful for low resolution, slitless spectroscopy in the far and near UV bands of a variety of cosmic sources such as hot stars, interacting binaries, active galactic nuclei, etc. We present calibration of these gratings using observations of UV standards NGC 40 and HZ 4. We perform wavelength and flux calibration and derive effective areas for different grating orders. We find peak effective areas of  $\sim 18.7 \text{ cm}^2$  at  $2325 \text{ \AA}$  for the  $-1$  order of NUV-Grating,  $\sim 4.5 \text{ cm}^2$  at  $1390 \text{ \AA}$  for the  $-2$  order of FUV-Grating1, and  $\sim 4.3 \text{ cm}^2$  at  $1500 \text{ \AA}$  for the  $-2$  order of FUV-Grating2. The FWHM spectral resolution of the FUV gratings is  $\approx 14.6 \text{ \AA}$  in the  $-2$  order. The  $-1$  order of NUV grating has an FWHM resolution of  $\approx 33 \text{ \AA}$ . We find excellent agreement in flux measurements between the FUV/NUV gratings and all broadband filters. We have generated spectral response of the UVIT gratings and broadband filters that can directly be used in the spectral fitting packages such as XSPEC, Sherpa and ISIS, thus allowing spectral analysis of UVIT data either separately or jointly with X-ray data from *AstroSat* or other missions.

**Keywords.** Ultraviolet astronomy – ultraviolet telescopes — ultraviolet detectors — calibration

## 1. Introduction

The Ultra-Violet Imaging Telescope (UVIT; Subramaniam *et al.* 2016; Tandon *et al.* 2017; Tandon *et al.* 2020) is one of the four co-aligned payloads onboard the Indian multi-wavelength space observatory *AstroSat* (Agrawal, 2006; Singh *et al.*, 2014). UVIT is a twin telescope system, one of them is designed to observe in the far ultra-violet band ( $1300 - 1800 \text{ \AA}$ ) and is known as the FUV channel. The second telescope utilizes a beam splitter that separates near UV and visible light, thus forming two detection channels – near UV (NUV;  $2000 - 3000 \text{ \AA}$ ) and visible (VIS;  $3200 - 5500 \text{ \AA}$ ). The three channels use identically configured intensified CMOS detector systems which only differ in having different photo-cathodes as per the wavelength band, and operate simultaneously. The beam splitter and the mechanical mounting of the telescopes cause the NUV channel field to be inverted and rotated by  $33^\circ$  with respect to the FUV channel field. Each channel is equipped with a set of filters that allow selection of bands with spectral coverage of  $\Delta\lambda \sim 125 \text{ \AA} - 500 \text{ \AA}$  (FUV),  $\Delta\lambda \sim 90 \text{ \AA} - 800 \text{ \AA}$  (NUV) and  $\Delta\lambda \sim 400 \text{ \AA} - 2200 \text{ \AA}$  (VIS). The FUV and NUV channels provide excellent imaging capability with a point spread function (PSF) in the range  $1 - 1.5 \text{ arcsec}$

(FWHM). The UVIT is mainly an imaging instrument with limited spectral capability. It can be used for low resolution, slitless spectroscopy in the far and near UV bands.

There are three UVIT gratings that are ruled with  $400 \text{ lines mm}^{-1}$  on CaF<sub>2</sub> substrates of  $4.52 \text{ mm}$  thickness. The dispersion in the detector plane caused by each grating is  $12 \text{ \AA arcsec}^{-1}$  and  $6 \text{ \AA arcsec}^{-1}$  in the first and second order, respectively, at  $1350 \text{ \AA}$ . One of three gratings is mounted on the NUV channel filter wheel while the other two gratings are mounted on the FUV channel filter wheel such that their dispersion axes are nearly perpendicular. Such an orthogonal arrangement of FUV gratings helps in avoiding contamination of nearby sources in the grating images. A source along the dispersion arm of the main target in one FUV grating image will cause contamination while the dispersion arms will be well separated in the other FUV grating image due to the orthogonal arrangement. The FUV gratings and the detector are designed to maximize the efficiency in the  $m = -2$  order while the NUV grating and the detector provide maximum efficiency in the  $m = -1$  order. The main parameters of the gratings are listed in Table 1. More details on UVIT gratings can be found in Tandon *et al.* (2017); Tandon *et al.* (2020). The UVIT gratings have been described with different

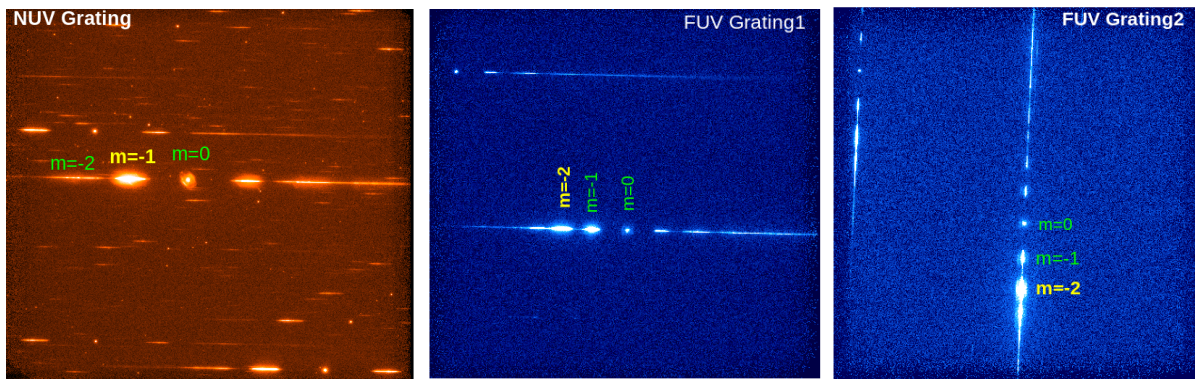


**Figure 1.** FUV/NUV Grating images of NGC40. The negative grating orders are marked. The image sizes are  $\sim 9.8$  arcmin on one side.

names, in Table 1 we list all the IDs to avoid any confusion when using different resources. Here we refer the gratings as FUV-Grating1 (FUV-G1), FUV-Grating2 (FUV-G2) and NUV-Grating (NUV-G).

In this paper, we present calibration of the UVIT gratings. Some of the results derived in this paper are presented in Tandon *et al.* (2020). Here, we present the calibration of the UVIT gratings, some results of which can be found in Tandon *et al.* 2020. Our updated work here results in minor changes to the wavelength and flux calibrations, and also includes additional grating orders. We describe the calibration method, derive additional calibration products and discuss cross-calibration between the gratings and broadband filters. The paper is organized as follows. We describe the UVIT data and the reduction in Sec. 2., extraction of one dimensional (1d) grating spectra in Sec. 3., and wavelength calibration in Sec. 4.. We derive effective areas and perform flux calibration in Sec. 5., and discuss cross-calibration between the gratings and broadband filters in Sec. 6. In Sec. 7., we derive instrumental response in the form of a product of redistribution matrix and ancilliary response that can be directly used in popular spectral fitting packages in X-ray astronomy. Finally we summarize our results in Sec. 8..

## 2. Calibration observations and data reduction

We used UVIT observations of NGC 40 and HZ 4, these observations are as listed in Table 2. The planetary nebula NGC 40 has a rich set of UV emission lines and is well suited for wavelength calibration. The white dwarf HZ 4 is a well-established spectrophotometric standard with nearly featureless spectrum, and is appropriate for flux calibration (e.g., Bohlin *et al.* 1990). HZ 4 has also been used for the photometric calibration of UVIT filters (Tandon *et al.*, 2017; Tan-

don *et al.*, 2020)

We used the Level1 data from the observations listed in Table 2. We used the UVIT pipeline CCDLAB (Postma & Leahy, 2017) to process the Level1 data. The pipeline performs corrections for field distortion, centroiding bias, flat field, pointing drift and accounts for frames rejected due to cosmic rays or missing from the level1 data. We used the VIS images to generate drift series which could then correct for the pointing drift in each orbit. We generated cleaned images for each orbit, aligned and merged them for each grating, as shown in Figure 1. The x,y coordinates in these images represent 1/8 subpixel coordinates. Hereafter, we refer to these 1/8 subpixels simply as pixels which are  $\approx 0.413$  arcsec wide. The images show the undispersed zeroth order image together with the dispersed  $\pm 1$  and  $\pm 2$  order two dimensional spectra. The dispersion axis for the FUV-G1 and NUV-G is nearly horizontal, while it is roughly vertical in the case of FUV-G2. The grating images show maximum intensity in the blazed order ( $m = -2$  for FUV gratings and  $m = -1$  for the NUV grating). The FWHM of the intensity distribution along the cross-dispersion direction is a measure of combined PSF due to the telescope, detector and grating. Since gratings introduce some distortions, the PSF is slightly broader ( $FWHM \sim 2$  arcsec) for grating images compared to that for the broadband filter images (Tandon *et al.*, 2017).

For the calibration and analysis of the UVIT data processed with the CCDLAB pipeline, we have developed a software package UVITTools in the Julia language (Bezanson *et al.*, 2012). We have used this package extensively here. We also used the FTOOLS<sup>1</sup>, Sherpa (Freeman *et al.*, 2001) and XSPEC (Arnaud, 1996) packages for generating response files and fitting

<sup>1</sup><https://heasarc.gsfc.nasa.gov/lheasoftware/>

**Table 1.** UVIT Grating parameters

Parameter	FUV-Grating1	FUV-Grating2	NUV-Grating
Filter Wheel Slot number	4	6	4
IDs in APPS	4 - grating1 (FUV)	6 - grating2 (FUV)	4 - grating (NUV)
IDs in CCDLAB	FUV_Grating1	FUV_Grating2	NUV_Grating
This paper	FUV-G1	FUV-G2	NUV-G
IDs in Tandon <i>et al.</i> (2020)	FUV1	FUV2	NUV
IDs in Tandon <i>et al.</i> (2017)	2nd FUV grating (#66126)	1st FUV grating (#63771)	NUV grating (#66125)
IDs in UVIT Pipeline	F4	F6	F4
$m = -1$ peak $\lambda$	–	–	2100Å
$m = -2$ peak $\lambda$	$\sim 1400\text{\AA}$	$\sim 1500\text{\AA}$	–
Spectral resolution (FWHM)	14.6Å	14.6Å	33Å

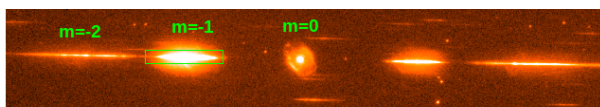


**Figure 2.** NUV Grating image of NGC 40 with the grating orders marked. The extent along the dispersion direction and the width along the spatial direction used to extract the 1d spectrum is shown as the rectangular region covering the  $m = -1$  grating order.

the data.

### 3. Extraction of 1d spectra

It is clear from Fig. 1 that the dispersion axes are not exactly aligned to either of the x or y axis. We measured the tilt angle relative to the x-axis and found that the dispersion axes can be represented by the linear relations  $y = mx + c$  where  $m = \tan\theta$ ,  $c = y_o - mx_0$  and  $x_0$  and  $y_0$  are the pixel coordinates of the centroid of the zero order image. We list the tilt angles in Table 3. The linear relations define the spectral trace i.e., the centroids of the cross-dispersion spatial profiles at each pixel on the dispersion axis. There is no additional significant distortion in the dispersion direction, so spatial profile fittings to trace the dispersion direction is not required.

We define coordinates along the dispersion direction as the pixel coordinates relative to the zero order position. We examined the grating images visually and determined the range of coordinates for different grating orders. These ranges are listed in Table 3. We used a 50 pixel width along the spatial direction centered on the trace defined by the linear relations and summed the counts to generate 1d spectra of a source of interest. Figure 2 shows the region used for the extraction of 1d spectrum of NGC 40 in the  $m = -1$  order. We also

extracted a 1d background spectrum from a source-free region in the image using the same relative coordinates in the dispersion direction and the same width along the spatial direction as used for the source. We subtracted the background counts from the source counts and propagated their errors on counts. The net 1d spectra of NGC 40 thus generated are shown in the left panels of Figure 3.

### 4. Wavelength Calibration

The raw 1d spectra shown in Figures 3 are not in physical units. In order to convert the relative pixel coordinates along the dispersion direction, we used the emission lines from NGC 40. We measured the emission line positions by fitting Gaussian profiles along with low order polynomial for the continuum. We then identified the strong emission lines in the UVIT spectra using the emission lines listed in Feibelman (1999) based on *IUE* observations. We then fitted the following linear relation between the line wavelengths and the relative pixel numbers.

$$\lambda(\text{\AA}) = a + bX, \tag{1}$$

where  $X$  is the pixel coordinate along the dispersion direction relative to the zero order position. The best-fit linear relations are shown in the right panels of Figures 3 for the blazed orders of FUV and NUV gratings. The slope and intercept of the best-fitting linear dispersion relation are listed in Table 3. We converted the pixel coordinates in the raw grating spectra to wavelength in Angstroms using the above dispersion relations.

### 5. Flux Calibration and Effective Area curves

Flux calibration is the process of converting the observed count rate to flux density as a function of wave-

**Table 2.** UVIT/Grating observations of NGC 40 and HZ 4

Target	ObsID	Date of Observation	Grating	Exposure Time (s)	window size
NGC 40	C02_010T01_900000	2016-12-07	FUV-G1	1194.0	350 × 350
			FUV-G2	1186.9	350 × 350
			NUV-G	2407.8	350 × 350
HZ 4	T01_054T01_9000000	2016-02-02	FUV-G1	1337.8	512 × 512
			FUV-G2	1026.2	512 × 512
			NUV-G	3082.9	512 × 512

**Table 3.** Parameters for 1d spectral extraction and the coefficients of the linear dispersion relation

Grating	Tilt angle ( $\theta$ )	Order	Range in relative Pixel coordinate (X)	Linear dispersion relation	
				Intercept ( $a$ )	Slope ( $b$ )
FUV-G1	358.703°	-2	-629 to -413	43.4	-2.791
	358.703°	-1	-323 to -213	-18.0	-5.833
FUV-G2	267.531°	-2	-624 to -426	31.2	-2.812
	267.531°	-1	-313 to -228	45.0	-5.625
NUV-G	358.904°	-1	-545 to -336	45.1	-5.523

**Table 4.** The coefficients of the best-fitting polynomials to the effective areas of UVIT gratings

Coefficient	FUV-G1		FUV-G2		NUV-G
	$m = -2$	$m = -1$	$m = -2$	$m = -1$	$m = -1$
$c_0$	53940.6148	-522747.0992	15052.4039	-1.2976	2.3671
$c_1$	-212.0132	2424.3078	-49.4344	0.0418	-0.0362
$c_2$	0.3446	-4.8004	0.0645	-0.00036	0.0011
$c_3$	-0.0003	0.0053	$-4.1806 \times 10^{-5}$	$1.3620 \times 10^{-6}$	$-5.1848 \times 10^{-6}$
$c_4$	$1.4266 \times 10^{-7}$	$-3.4478 \times 10^{-6}$	$1.3476 \times 10^{-8}$	$-2.2112 \times 10^{-9}$	$1.08550 \times 10^{-8}$
$c_5$	$-3.6369 \times 10^{-11}$	$1.3509 \times 10^{-9}$	$-1.7298 \times 10^{-12}$	$1.2713 \times 10^{-12}$	$-1.19142 \times 10^{-11}$
$c_6$	$3.8411 \times 10^{-15}$	$-2.9306 \times 10^{-13}$	–	–	$6.5940 \times 10^{-15}$
$c_7$	–	$2.7159 \times 10^{-17}$	–	–	$-1.4486 \times 10^{-18}$
$\lambda_0$	0.0	0.0	0.0	1250.0	1900.0

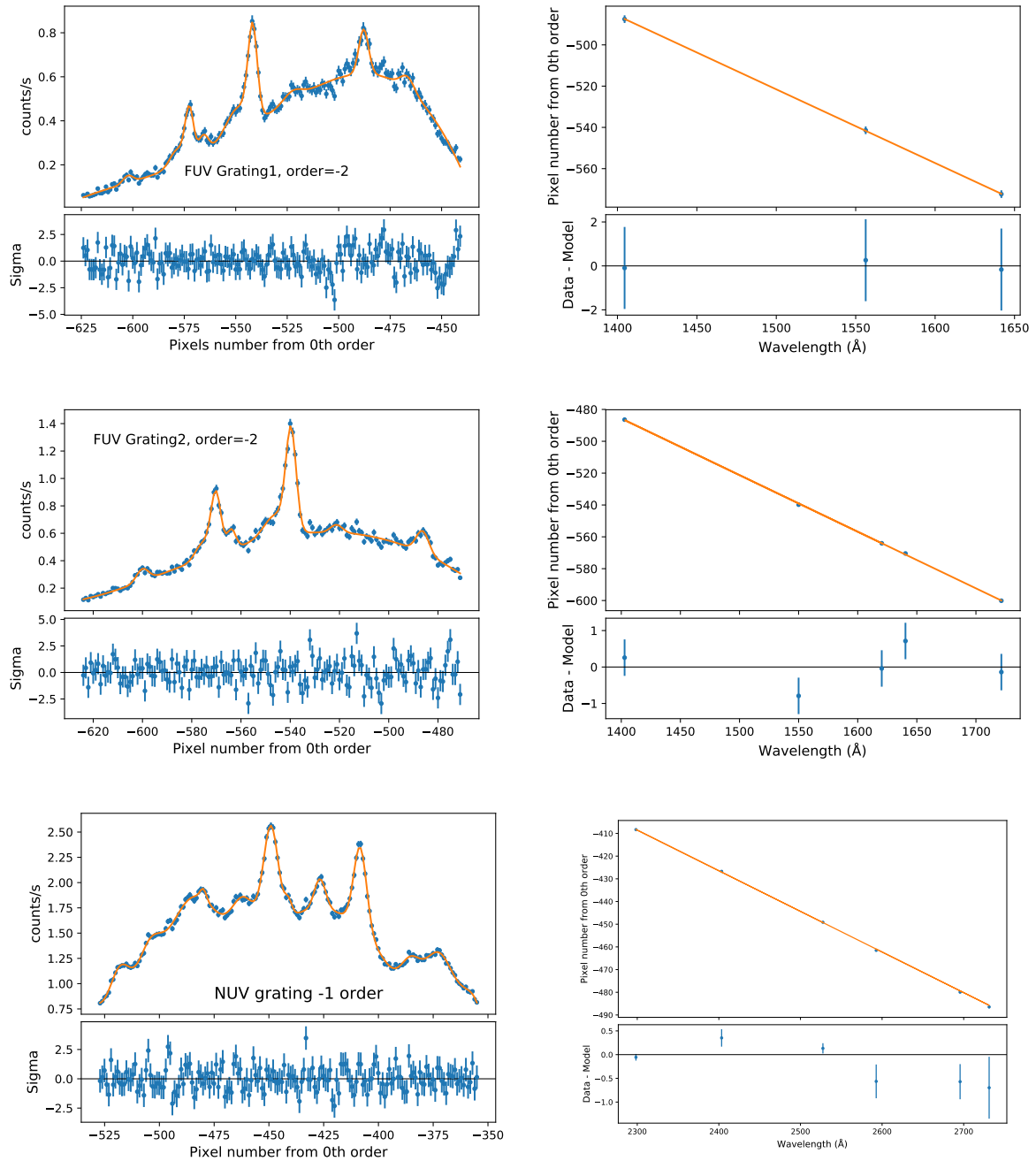


**Figure 3.** The UVIT grating spectra of NGC 40 (left panels) and pixel-wavelength calibration (right panels) of the blazed orders (top panels: FUV-G1,  $m = -2$ ; middle panels: FUV-G2,  $m = -2$ , bottom panels: NUV-G,  $m = -1$ ). The 1d spectra i.e., count rate Vs pixel numbers from the centroid of the 0th order, are fitted with a number of Gaussian profiles for the emission lines and polynomial for the continua.

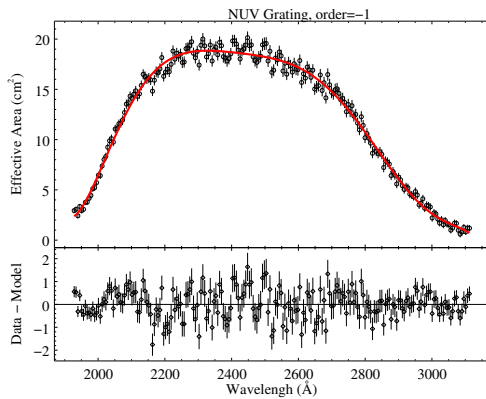


**Figure 4.** The  $m = -1$  order NUV Grating effective area, the best-fitting polynomial and the residuals.

length. The background-subtracted net count rate is related to the incident flux density  $f_\lambda$  [ergs cm<sup>-2</sup> s<sup>-1</sup> Å<sup>-1</sup>] as

$$C(X) = \int R_{X\lambda} A_\lambda f_\lambda \left( \frac{\lambda}{hc} \right) d\lambda \quad (2)$$

where  $C(X)$  is the net count rate at  $X$  along the dispersion direction,  $R_{X\lambda}$  gives the probability that a UV photon of wavelength  $\lambda$  gets detected at  $X$ ,  $A_\lambda$  is effective area of the spectrometer accounting for the collecting area of the telescope, reflectivity of the mirrors, grating efficiency, detector quantum efficiency and attenuation efficiency of any other optical element. Thus  $A_\lambda$  is telescope area corrected for all losses. In principle,  $A_\lambda$  can be determined from pre-launch lab measurements, however, the various efficiencies generally change with time during and after launch. Hence,  $A_\lambda$  is generally determined or corrected based on observations of standard sources with well measured fluxes. Eqn. 2 is appropriate for the photon counting data from UVIT, and can be written in matrix form with  $\lambda$ ,  $X$  now representing wavelength and spectral bins,

$$C_X = \sum_\lambda R_{X\lambda} A_\lambda f_\lambda \frac{\lambda}{hc} \quad (3)$$

In the case of dispersive spectrometers such as the FUV/NUV gratings with suppression of order-overlap, the response matrix can be assumed to be diagonal. Hence  $R_{X\lambda} = 1$  if  $\lambda$  and  $X$  follow the dispersion relation. Thus,

$$f_\lambda = \frac{C_\lambda (hc/\lambda)}{A_\lambda}, \quad (4)$$

where  $C_\lambda$  is the count rate spectrum.

To determine the effective areas of the gratings, we used the UVIT grating observations of spectrophotometric standard HZ4 (whose UV spectral flux values were obtained from spectrum file `hz4_stis_005.fits` available at HST-CALSPEC<sup>2</sup>). We matched the wavelengths bins of  $C_\lambda$  measured with UVIT gratings and the spectrum by linearly interpolating the standard spectrum. One can then calculate the effective area of the UVIT-gratings using Eqn. 4. However, we note that HZ 4 shows strong absorption lines at 1216Å (*Lyα*) and 1400Å, and the spectral resolution of the standard spectrum measured with *IUE* in the far UV band is superior compared to that of the UVIT grating spectra. We therefore smoothed the HZ4 standard spectrum to match the UVIT grating spectral resolution. We used Gaussian kernels with widths that resulted in smooth effective areas using Eqn. 4 for different grating orders. The effective areas thus derived are shown in Figure 4 for the  $-1$  order of NUV-G, and in Figure 5 for the  $-2$  orders of FUV-G1 and FUV-G2.

We have fitted the UVIT-grating effective areas with low order polynomials of the form  $A_\lambda = \sum c_n (\lambda - \lambda_0)^n$  so that the observed count rate spectrum can be converted to the fluxed-spectrum by dividing the best-fitting polynomials using Eqn. 4. The best-fitting coefficients are listed in Table 4, and the best-fitting polynomials are shown in Fig. 4 and Fig. 5.

## 6. Cross-calibration between gratings and broadband filters

The flux densities measured by broadband filters at their mean wavelengths must be the same as those measured by the gratings at the same wavelengths if the mean wavelengths represent the effective wavelengths of the filters. Small discrepancies may be expected as the mean wavelengths of the UVIT filters are not defined to fulfil the above condition (private communication with S. N. Tandon). Nevertheless it is useful to compare the flux measured with the gratings and broadband filters. As mentioned earlier, gratings introduce distortion making the PSF slightly poorer. Hence, the same sizes for the extraction regions i.e., the spatial width along the cross-dispersion direction in the case of grating observations and the diameter of the circular region in the case of broadband filter observations, may not provide the same flux densities. Therefore it is important to cross-calibrate the gratings and the broadband filters.

<sup>2</sup><http://www.stsci.edu/hst/observatory/cdbs/calspec.html>

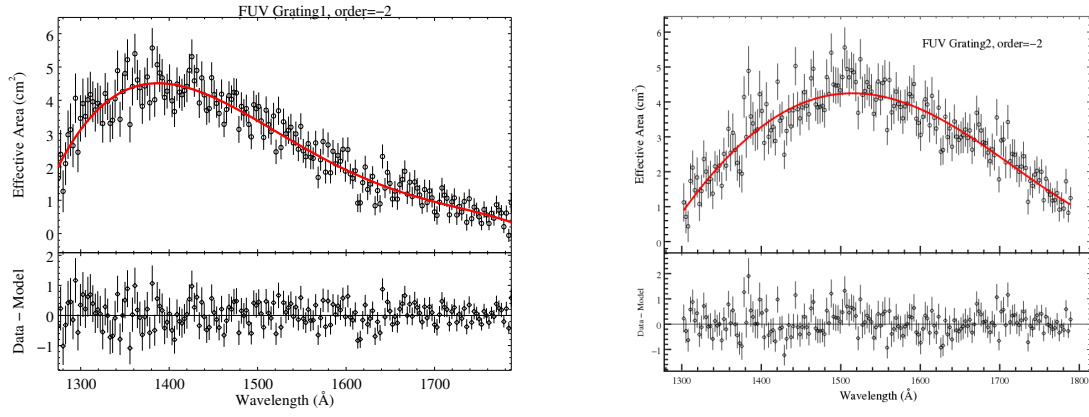


**Figure 5.** The  $m = -2$  order FUV Grating1 and Grating2 effective areas, the best-fitting polynomials and the residuals.

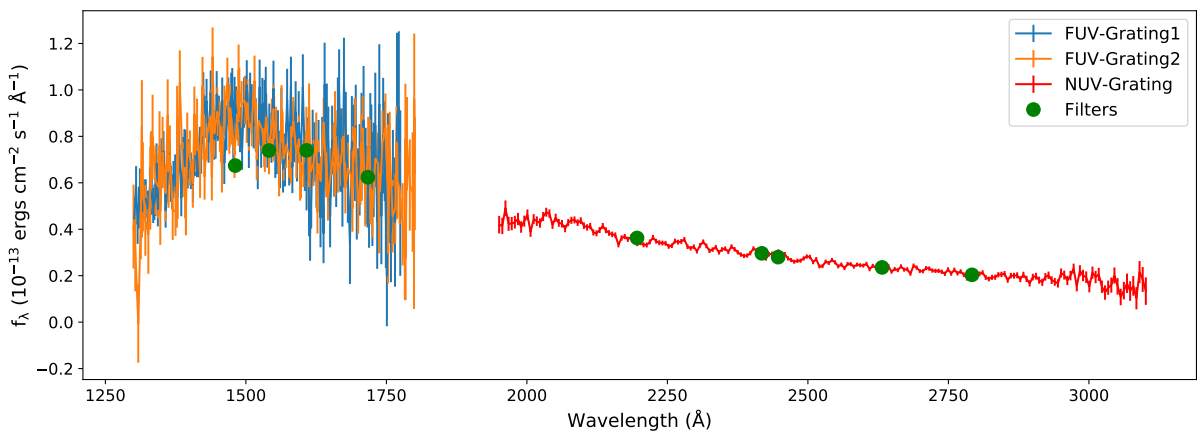


**Figure 6.** A comparison of flux densities at various wavelengths derived from the FUV/NUV broadband filters and grating observations of HZ 4.

For this purpose, we used the calibration information and count rates already derived by Tandon *et al.* (2020). For HZ 4, we used their corrected count rates that were derived after applying corrections for flat field and saturation effects. We converted these count rates to flux densities using the unit conversion (UC) factors which we calculated from the ZP magnitudes listed in Table 3 of Tandon *et al.* (2020). We derived the UC factors from the ZP magnitude as follows (Tandon *et al.*, 2017),

$$UC = 10^{-0.4 \frac{(ZP+2.407)}{\lambda_{mean}^2}}, \quad (5)$$

where UC is in  $\text{ergs cm}^{-2} \text{s}^{-1} \text{\AA}^{-1}$  and  $\lambda_{mean}$  is in  $\text{\AA}$ . The flux density  $f_\lambda$  in  $\text{ergs cm}^{-2} \text{s}^{-1} \text{\AA}^{-1}$  is

$$f_\lambda = CPS \times UC, \quad (6)$$

where CPS is the count rate in  $\text{counts s}^{-1}$ . In Table 5, we list the net count rate from (Tandon *et al.*, 2020), the UC factors and flux density calculated using Eqn. 5 and Eqn. 6 for HZ 4.

In order to check possible calibration differences between the flux densities derived from the gratings and broadband filters, we plot FUV/NUV grating spectra and flux densities derived for different filters in Figure 6. It is clear that, except for the F148W (CaF2-1) filter, the flux measurements agree very well between the gratings and the broadband filters. The F148W flux density is  $\sim 25\%$  lower compared to that measured with the FUV gratings. The discrepancy is at a level of  $2.4\sigma$ . In comparison to the standard spectrum (hz4\_stis\_005.fits) used for the calibration of gratings, the F148W flux density is also lower by  $\sim 21\%$ . This apparent discrepancy is most likely due to the presence of sharp spectral features in the standard spectrum near the mean wavelength of the F148W filter. The spectral features are not well resolved by the FUV gratings. To further check, we calculated the expected count rates of HZ 4 using Eqn. 2 based on the effective areas from (Tandon *et al.*, 2020) and the FUV-G1 and NUV-G spectra. The predicted count rates are listed in Table 5. It is clear that the observed and predicted count rates agree very well. This shows the importance of using effective areas as discussed below. Based on the above analysis, we recommend a cross-dispersion width of 50 pixels for spectral extraction of point sources. In case of poor tracking correction and extended sources, a larger cross-dispersion width should be used.

## 7. Grating spectral responses and multi-wavelength spectroscopy

Working with data from different instruments onboard *AstroSat* require tools and techniques to facilitate joint analysis of multi-wavelength data. In particular, the broadband spectral coverage of *AstroSat*, from near UV to hard X-rays, requires tools for simultaneous fitting of spectral models to the multi-wavelength data. Due to the complex interactions when X-rays go through the detector material, the response function of X-ray detectors are generally complex, and the X-ray spectral data cannot be directly converted to the source spectrum. X-ray spectral analysis begins with an assumed source spectral model which is then folded with the instrument response that results in model spectral data which is then compared with the observed spectral data. The source spectrum is thus inferred from the best-fitting model. Grating spectrometers, such as the UVIT gratings, have much simpler response functions, and one generates a fluxed spectrum directly from the observations using the dispersion relation and the wavelength-dependent effective area or sensitivity curve as described in the previous section. The source spectral properties are inferred from the fluxed spectrum after correcting for the instrumental spectral resolution. It is possible to treat the photon counting data from UVIT similar to the X-ray data that are also photon counting by generating appropriate spectral responses in the form of a redistribution matrix (RMF) and ancillary response file (ARF), and use Eqn. 7 below which is similar to Eqn. 2 to infer the source spectrum. One can then perform joint spectral analysis of UVIT and X-ray data from SXT, LAXPC and CZTI. In the following, we generate the count spectrum (i.e., distribution of photon counts in different spectral channels), redistribution matrix and ancillary response for UVIT gratings and broadband filters. Such an approach is more accurate than directly converting the count rates to flux densities with unit conversion factors and zero point magnitudes for various filters as the latter quantities depend on the spectral shape. The unit conversion factors and zero point magnitudes are derived for the particular spectral shape of the spectrophotometric standard HZ 4 and are unlikely to be strictly correct for objects with different spectral shape.

For the UVIT gratings, we constructed a count spectrum (counts vs spectral channels) from the uncalibrated 1d spectrum (counts vs relative pixel coordinates) in the same format as the X-ray spectral PHA files. For this purpose, we added a positive integer number to the relative pixel coordinate and converted to spectral channels (I) which start from 1. This count spectrum is related to the source spectrum in a way sim-

**Table 5.** The unit conversion factor (UC) for UVIT filters, and the observed count rate, flux density and predicted count rate for HZ 4 in different filters.

Filter	$\lambda_{mean}$ (Å)	UC (ergs cm <sup>-2</sup> s <sup>-1</sup> Å <sup>-1</sup> )	Obs. CPS <sup>a</sup>	HZ 4 $f_{\lambda}$ <sup>b</sup>	Pred. CPS <sup>c</sup>	
F148W	CaF2-1	1481	$(2.866 \pm 0.026) \times 10^{-15}$	23.5	$6.741 \pm 0.062$	$21.5 \pm 1.3$
F154W	BaF2	1541	$(3.574 \pm 0.033) \times 10^{-15}$	20.7	$7.392 \pm 0.068$	$19.1 \pm 1.4$
F169M	Sapphire	1608	$(4.57 \pm 0.0427) \times 10^{-15}$	16.2	$7.397 \pm 0.068$	$15.5 \pm 1.2$
F172M	Silica	1717	$(1.143 \pm 0.021) \times 10^{-14}$	5.5	$6.24 \pm 0.11$	$5.7 \pm 0.8$
N242W	Silica-1	2418	$(2.3179 \pm 0.0043) \times 10^{-16}$	127.8	$2.9622 \pm 0.0055$	$131.6 \pm 1.2$
N219M	NUVB15	2196	$(4.924 \pm 0.091) \times 10^{-15}$	7.4	$3.624 \pm 0.067$	$7.5 \pm 0.1$
N245M	NUVB13	2447	$(7.571 \pm 0.035) \times 10^{-16}$	37.0	$2.799 \pm 0.013$	$37.8 \pm 0.3$
N263M	NUVB4	2632	$(8.674 \pm 0.080) \times 10^{-16}$	27.2	$2.356 \pm 0.022$	$27.6 \pm 0.4$
N279N	NUVN2	2792	$(3.793 \pm 0.035) \times 10^{-15}$	5.4	$2.037 \pm 0.019$	$5.5 \pm 0.1$

<sup>a</sup> Observed count rate in counts s<sup>-1</sup>. Errors on the observed CPS are less than 2%.

<sup>b</sup> In unit of 10<sup>-14</sup> ergs cm<sup>-2</sup> s<sup>-1</sup> Å<sup>-1</sup>.

<sup>c</sup> Predicted count rate using the effective areas provided in (Tandon *et al.*, 2020) and the FUV-G1 and NUV-G spectra of HZ 4 shown in Fig. 6.

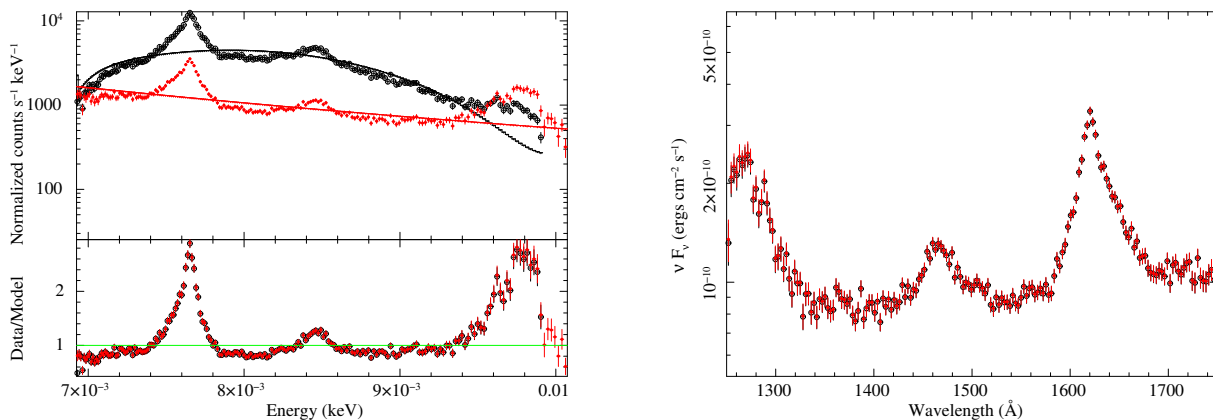


**Figure 7.** Comparison of count PHA spectrum of Fairall 9 with instrument response and fluxed PHA spectrum with diagonal response. *Left panels:* Count PHA data (black open circles), flux PHA data (red filled circles), the same powerlaw fitted to the both datasets and the data-to-model ratios. *Right panel:* Unfolded spectra using a powerlaw of photon index,  $\Gamma = 0$  ( $N_E = A E^{-\Gamma}$ ) and unit norm at 1 keV. Both the count PHA and fluxed spectra were extracted from the  $-2$  order of FUV-G2 image.

ilar to Eqn. 2,

$$D(I) = T \int R(I, E)A(E)N_E dE + B(I), \quad (7)$$

where  $D(I)$  is the source + background count in spectral channel  $I$ ,  $B(I)$  is the background counts in channel  $I$ ,  $T$  is exposure time.  $R(I, E)$  is the redistribution matrix and  $A(E)$  is effective area at energy  $E$ ,  $N_E$  is the photon spectrum of the source.

The redistribution matrix  $R(I, E)$  represents the spectral response which is Gaussian with an FWHM that is the same as the spectral resolution of the grating spectrometers. To measure the spectral resolution of UVIT gratings, we fitted Gaussian profiles to the emission lines observed from NGC 40 and derived the FWHM= 14.63Å (FUV gratings,  $m = -2$ ), 33Å (NUV-G,  $m = -1$ ). In order to generate the response matrix for the NUV-G, we divided the wavelength range in 2341 energy bins. For each energy bin, we generated the Gaussian response in 210 channels which were defined based on the dispersion solution. We also multiplied the effective area with the redistribution matrix as in Eqn. 7 and created the grating response matrix which is the product  $R(I, E)A(E)$ . The responses thus created for each calibrated grating order are compatible with the X-ray spectral fitting packages such as XSPEC (Arnaud, 1996), Sherpa (Freeman *et al.*, 2001) and ISIS (Houck & Denicola, 2000). The source and background PHA files along with the spectral response can directly be used in one of the above spectral fitting packages. This is helpful for joint UV/X-ray spectral modeling. We also created single channel response matrices for the broadband filters using the updated effective areas provided in Tandon *et al.* (2020). These response files along with the grating or filter spectral PHA data in the fits format give complete flexibility to treat and analyze the photon counting UVIT data in a way similar to the X-ray photon counting data.

Another way to use the UV grating spectra and photometric flux in the joint UV/X-ray spectral analysis is to convert the fluxed spectra in PHA format and generate diagonal responses using the FTOOLS package. However, this has the disadvantage of not considering the actual spectral response of the instrument. Hence, the uncertainty associated with the UC factor for the particular spectral shape of the standard star for a given broadband filter will enter into the spectral fitting. In the case of grating spectra, the derived spectral line widths will not be free of instrumental resolution as the instrument spectral response is not being used.

We demonstrate the equivalence of these two approaches as follows. For this purpose we used UVIT grating observations of a Seyfert 1 AGN Fairall 9 (ObsID: G06\_157T01\_9000000). We processed the Level1

data in the same way as in the case of NGC 40 and HZ 4. We generated an  $m = -2$  order FUV-G2 spectrum of Fairall 9 in the PHA format. We also generated the associate background spectrum from the source-free regions as described earlier, and updated the PHA header of the source spectral file to include the grating response and the background spectral file. We loaded these spectral data into XSPEC and plotted the spectral data as shown in Figure 7. We also generated a fluxed spectrum i.e.,  $f_\lambda$  Vs  $\lambda$  of Fairall 9 for the FUV-G2 in the  $m = -2$  order and converted these data to PHA file and diagonal response matrix using FTOOLS. The two spectra of Fairall 9 are compared in Fig. 7. It is clear that the two approaches agree well.

## 8. Summary & Conclusion

We calibrated the two FUV gratings in the orders  $-2$  and  $-1$  and one NUV grating in the  $-1$  order. We derived dispersion solutions and effective areas for the grating orders which can be used for spectral calibration of any source observed with the UVIT gratings. We also checked the cross-calibration between the gratings and broadband filters and found excellent agreement in flux measurements for all broadband filters except the FUV filter F148W. We provide the updated UC and ZP for this filter. We also generated the spectral response files for the gratings and the broadband filters that can be directly used for spectral analysis using XSPEC, Sherpa or ISIS. A software package UVITTools for the analysis of UVIT data processed with the CCDLAB pipeline has been developed.

## Acknowledgments

The author is grateful to Shyam Tandon for numerous discussions on various aspects of UVIT, and allowing to use the calibration data. The author is thankful to Phil Charles and Shyam Tandon for their suggestions on the submitted version of the manuscript. This publication uses the data from the AstroSat mission of the Indian Space Research Organisation (ISRO), archived at the Indian Space Science Data Centre (ISSDC). This publication uses UVIT data processed by the payload operations centre at IIA. The UVIT is built in collaboration between IIA, IUCAA, TIFR, ISRO and CSA.

## References

- Agrawal, P. C. 2006, *Advances in Space Research*, 38, 2989

- Arnaud, K. A. 1996, in *Astronomical Society of the Pacific Conference Series*, Vol. 101, *Astronomical Data Analysis Software and Systems V*, ed. G. H. Jacoby & J. Barnes, 17
- Bezanson, J., Karpinski, S., Shah, V. B., & Edelman, A. 2012, arXiv e-prints, arXiv:1209.5145
- Bohlin, R. C., Harris, A. W., Holm, A. V., & Gry, C. 1990, *ApJS*, 73, 413
- Feibelman, W. A. 1999, *ApJ*, 514, 296
- Freeman, P., Doe, S., & Siemiginowska, A. 2001, in *Society of Photo-Optical Instrumentation Engineers (SPIE) Conference Series*, Vol. 4477, *Astronomical Data Analysis*, ed. J.-L. Starck & F. D. Murtagh, 76–87
- Houck, J. C., & Denicola, L. A. 2000, in *Astronomical Society of the Pacific Conference Series*, Vol. 216, *Astronomical Data Analysis Software and Systems IX*, ed. N. Manset, C. Veillet, & D. Crabtree, 591
- Postma, J. E., & Leahy, D. 2017, *PASP*, 129, 115002
- Singh, K. P., Tandon, S. N., Agrawal, P. C., *et al.* 2014, in *Society of Photo-Optical Instrumentation Engineers (SPIE) Conference Series*, Vol. 9144, *Proc. SPIE*, 91441S
- Subramaniam, A., Tandon, S. N., Hutchings, J., *et al.* 2016, in *Society of Photo-Optical Instrumentation Engineers (SPIE) Conference Series*, Vol. 9905, *Space Telescopes and Instrumentation 2016: Ultraviolet to Gamma Ray*, ed. J.-W. A. den Herder, T. Takahashi, & M. Bautz, 99051F
- Tandon, S. N., Subramaniam, A., Girish, V., *et al.* 2017, *The Astronomical Journal*, 154, 128
- Tandon, S. N., Postma, J., Joseph, P., *et al.* 2020, *AJ*, 159, 158